# Mass Transfer in Fibrous Media with Varying Anisotropy for Flow Battery Electrodes: Direct Numerical Simulations with 3D X-ray Computed Tomography

Matthew D. R. Kok[1], Rhodri Jervis[2], Tom G. Tranter[3], Mohammad A. Sadeghi[1], Dan J. L. Brett[2], Paul R. Shearing[2], Jeff T. Gostick[3*]

[1]Department of Chemical Engineering, McGill University, Montreal, Canada

[2]Electrochemical Innovation Lab, Department of Chemical Engineering, University College London, UK

[3]Porous Media Engineering and Analysis Lab, Departments of Chemical Engineering, University of Waterloo, Canada

*corresponding author, present address: Engineering 6, University of Waterloo, 200 University Avenue West, Waterloo, ON N2L 3G1, Canada

Declaration of interests: none

## Abstract

A numerical method for calculating the mass transfer coefficient in fibrous media is presented. First, pressure driven flow was modelled using the Lattice Boltzmann Method. The advection-diffusion equation was solved for convective-reacting porous media flow, and the method is contrasted with experimental methods such as the limiting current diffusion technique, for its ability to determine and simulate mass transfer systems that are operating at low Reynolds number flows. A series of simulations were performed on three materials; specifically, commercially available carbon felts, electrospun carbon fibers and electrospun carbon fibers with anisotropy introduced to the microstructure. Simulations were performed in each principal direction (x,y,z) for each material in order to determine the effects of anisotropy on the mass transfer coefficient. In addition, the simulations spanned multiple Reynolds and Péclet numbers, to fully represent highly advective and highly diffusive systems. The resulting mass transfer coefficients were compared with values predicted by common correlations and a good agreement was found at high

Reynolds numbers, but less so at lower Reynolds number typical of cell operation, reinforcing the utility of the numerical approach. Dimensionless mass transfer correlations were determined for each material and each direction in terms of the Sherwood number. These correlations were analyzed with respect to each materials' permeability tensor. It was found that as the permeability of the system increases, the expected mass transfer coefficient decreases. Two general mass transfer correlations are presented, one correlation for isotropic fibrous media and the other for through-plane flow in planar fibrous materials such as electrospun media and carbon paper. The correlations are $Sh = 0.879\ Re^{0.402}\ Sc^{0.390}$ and $Sh = 0.906\ Re^{0.432}\ Sc^{0.432}$ respectively.

## Keywords:

Electrospun electrodes; Numerical modelling; X-ray computed tomography; Redox flow battery; Mass transfer coefficient; Fibrous media

## 1. Introduction

Understanding the mass transfer properties of porous electrodes is vital for the optimized operation of many electrochemical energy conversion and storage technologies. Overpotential due to mass transfer losses is caused by the inability to deliver adequate reactants to the surface of the electrode. As the overpotential of the cell increases, the overall efficiency is reduced. Considerable research has attempted to understand and quantify both the mass transfer coefficient and the effect it has on electrochemical performance. The effect of mass transport has been studied in redox flow batteries [1–3], direct methanol fuel cells [4] and solid oxide iron air batteries [5] among others. The present work focuses on quantifying the mass transfer coefficient in flow batteries, specifically addressing mass transfer to fibrous carbon electrodes in advective-diffusive systems. Kinoshita and Leach have proposed several correlations stemming from experiments on bromine systems with varying electrode thickness [6]. More recently, You et al. presented the results of similar experiments with an iron-based electrolyte [7] and Xu and Zhao looked at the mass transfer coefficient in a vanadium flow battery system [8,9]. Milshtein et al. recently published their investigation into the effect the mass transfer coefficient has on flow battery performance [10]. Most mass transfer investigations are conducted using the limited current diffusion technique (LCDT), where the electrode is operated at limiting current (i.e. under mass transfer control); thus the current is equal to the mass transfer rate. At limiting current conditions, the electrolyte concentration at the surface of the fibers is zero, and it is assumed that the bulk concentration is constant, allowing the mass transfer coefficient for the system to be determined by applying the film theory of mass transfer

[11]. Although LCDT is widely used, it does have limitations in the context of fibrous electrodes, especially high-performance materials such as electrospun mats [12]. To assure the bulk concentration is constant throughout the length of the electrode the electrolyte velocity must be sufficiently high. This precludes being able to effectively determine the mass transfer properties of systems with low Reynolds number (Re), such as Stokes flow which represents typical flow conditions in a flow battery assembly, and/or materials with very small length scales below 100 μm. In other words, current flow battery models are using correlations well outside their range of validity. For purposes of this work a low Reynolds number system will be Re $\leq 10^{-3}$ and a high Reynolds number system will be Re $> 10^{-1}$. For all uses in this article the Reynolds number is defined according to Eq. 15, using the superficial velocity and the fiber diameter as the characteristic length. Exacerbating this issue, recent work by our group [12] presented a promising electrode material made by electrospinning that has even smaller length scales (<1 μm), and thus even lower Re. The present work addresses this issue by outlining a method for determining the mass transfer coefficient in low Reynolds number flows in micro-fibrous media, by performing numerical simulations on high-resolution 3D computed tomography images of electrodes (a technique that has recently been applied to flow battery electrode materials [13–18]). This approach still has the issue of changing bulk concentration, but it is possible to devise simulation conditions that minimize this effect, and moreover, direct access to the spatial distributions of all properties in the simulation enables detection and/or accounting for any discrepancies. Similar studies have been conducted using direct numerical simulation on images, but they were performed on structured computer generated materials in two dimensions [19,20]. Applying these simulation conditions to real materials in 3D provides important insights into the mass transfer process in fibrous electrodes. A key component to this study is determining the effect of fiber anisotropy on the mass transfer coefficient. Cussler [21] and Yang and Cussler [22] have presented different correlations depending on the direction of the flow relative to the fibrous material. In structured fibrous electrodes, the alignment of the fibers in different planes will have a significant effect on the mass transport of the system and therefore the performance of the cell.

## 2. Methods and Materials

### 2.1. Materials

The electrospun materials were prepared on a custom electrospinning setup and carbonized in-house as previously reported [12,23]. The spin dope consisted of 12 wt% polyacrylonitrile (Sigma, MW 150,000) dissolved in N,N-dimethylformamide (Sigma, 99.8%). Standard electrospun materials were made by

electrospinning on a slowly rotating collector drum with a rastering needle to ensure an even membrane thickness. Anisotropic materials were made in the same manner, but by increasing the velocity of the rotating drum collector [24] which imparted noticeable alignment on the fibers. Commercially available carbon felts (GFD, SGL Group) were also obtained as a baseline comparison. These carbon felts feature bundles of carbon fibers entangled together in a weave to form a continuous material. While the bundles themselves may feature high degrees of anisotropy the material is nearly isotropic, and there would be no expectation of differing material properties whether measured in x, y or z directions. In the isotropic electrospun material, it was expected that the material properties would differ between the through-plane (z) direction and the in-plane directions (x,y). The random orientation of the fibers should ensure that the two in-plane directions are relatively similar. Electrospun materials with aligned fibers should have different transport phenomena in the through-plane and both in-plane directions. In the limit of perfect alignment, the through-plane direction should have the same properties as the in-plane, cross-fiber direction. Perfect alignment was not achieved here, but it was expected that the through-plane and cross-fiber directions would start to converge.

## 2.2. X-ray Tomography

Imaging of the electrospun materials, as well as the carbon felts, was performed on Zeiss Xradia Versa 520 micro-CT instrument (Carl Zeiss XRM, Pleasanton, CA). The instrument utilizes a two-stage magnification system which couples geometrical magnification with an optically coupled scintillator, More information on the instrument can be found elsewhere [25]. A 20× objective lens was employed for the scans of the two electrospun materials; using a low source voltage and sample diameter of 1 mm or less was required to obtain a good quality image due to the highly porous and low-Z nature of the mats. The samples were rotated through 360° and 1601 and 2201 projections of 30 s and 46 s exposure each were recorded for the unaligned and aligned materials, respectively. The resulting tomogram yielded a voxel size of 0.312 μm for the aligned material and 0.360 μm for the unaligned materials.

The carbon felt has much larger fiber diameters, and structural heterogeneities on a larger scale than the electrospun materials, and therefore the larger field-of-view, and larger pixel size of the 4× objective, was chosen. The 3D volume of the commercial felts used in this study is taken from a recent compression study that used an in-situ compression stage that has an attenuating glassy carbon tube architecture [17]. Therefore, a source voltage of 80 kV was required to give sufficient counts with a reasonable exposure time. 2401 projections of 40 s were obtained through a sample rotation of 360°, resulting in a voxel size of 1.79 μm. A filtered back-projection reconstruction algorithm (XM Reconstructor, Zeiss) was used to

reconstruct the X-ray transmission images into 3D tomograms. Reconstructed 3D images of the materials can be seen in Figure 1.

## 2.3.Quantitative Image Analysis

Quantifying the degree of anisotropy in fibrous materials is often performed qualitatively in two dimensions by visually analyzing SEM micrographs of the material. Basic image analysis can also provide a quantitative measure of the fiber alignment; however, this method is limited to either the top or the bottom of the material, as SEM is limited to a single plane or view.  3D tomograms provide an unprecedented opportunity to analyze material microstructures.  In this work, the fiber alignment was of specific interest: to quantify this, the chord-length distribution was employed [26] in the three principal directions. Chords refer to straight lines drawn in a given phase (either solid or void), and their length probes the feature size.  The main advantage of chords is that they are oriented in a given direction, so differences in chord lengths (or chord length distribution) indicate elongation of the phase-space in a certain direction. An example of chords applied to the electrospun material can be seen in Figure 2. Here the blue, red, and green lines represent chords drawn in the x, y and z directions, respectively, in the pore space. The grey lines shown in the cutout in the center of the image show chords drawn in all three directions in the fiber space. Analyzing the distributions of the chord lengths throughout the entire 3D volume, categorized by direction, can give an idea of the alignment present in the material. For example, for an unaligned electrospun material, the z peak of the chord-length distribution on the fibers should show a distinct peak at the diameter of the fibers, as this is the maximum distance any one chord should have. The x and the y peaks should be less severe and have a mean larger than the fiber diameter, representing the randomness of the alignment in those directions. These distributions should also have similar shapes (width and general structure).

Another key metric was the fiber diameter, which was used as the characteristic length in all dimensionless correlations presented below. This was obtained by applying a local thickness filter to the fiber phase and taking the fiber diameter as the peak of the local thickness histogram.  A local thickness filter assigns a numerical value to each voxel that is the radius of a largest sphere that both overlaps the voxel and fits entirely within the phase of interest.  This is different from the more commonly used distance transform, which is the radius of a sphere that is centered on the voxel. On its own, the distance transform is insufficient to determine an average fiber size. There would be a severe skewing towards the smaller sizes regardless of the size of the fiber.

The fiber diameter was selected as the characteristic length largely for reasons of practicality as it is the only pore-scale feature that is consistent throughout the materials and it also easily obtained. The more traditional definition of the hydraulic diameter for irregular internal flow would be $4A/P$ [27] but due to the complex nature of fibrous media and voxelated nature of the images, the area and wetted perimeter are almost impossible to accurately measure or calculate. Other characteristic lengths can be just as tricky to define, such as the average pore diameter or the average particle path which are highly variable. The most sensible method is to use the fiber size, and treat the system as external flow, which uses the obstacle size to determine the characteristic length. The use of fiber diameter also corresponds with the convention in the highly used Carman-Kozeny equation [28].

## 2.4. Lattice Boltzmann Simulations

Pressure-driven viscous flow was simulated in the materials using the Lattice Boltzmann Method (LBM) [29]. This numerical model was implemented using the open-source LB solvers Palabos [30] and Sailfish FD [31], using a 3D D3Q19 single relaxation time model with the standard Bhatangar-Gross-Krook (BGK) collision operator. The initial conditions held the velocity at zero everywhere and the fluid movement was initialized by applying a fixed pressure gradient between the inlet and the outlet [32]. A variety of pressure gradients were implemented to ensure a representative number of flow conditions were represented.

## 2.5. Direct Numerical Simulation

The advection-diffusion equation (Eq. 1) describes the dispersion of an electrolyte due to advective and diffusive forces in a reacting system. Direct implementation of the equation only allows systems with homogenous reactions; however, when applied to voxel images as done here, the boundary conditions at the fluid-solid interface can be modified to represent a heterogeneous reacting system.

$$\frac{\delta C}{\delta t} = \vec{\nabla} \cdot \left( D \vec{\nabla} C \right) - \vec{\nabla} \cdot (\vec{v} C) + R \qquad\qquad 1$$

where $C$ is the concentration of the electrolyte [mol·m$^{-3}$], $D$ is the binary diffusivity [m$^2$·s$^{-1}$] and $v$ is the component velocities of the flow field [m·s$^{-1}$]. It was assumed the process is at steady state, the diffusivity of the reactant was constant throughout the domain regardless of local concentration and there is no homogenous reaction occurring in the bulk ($R = 0$). These assumptions reduce Eq. 1 to the following:

$$D\vec{\nabla}^2 C - \left( C \cdot \vec{\nabla}\vec{v} + \vec{v} \cdot \vec{\nabla} C \right) = 0 \qquad\qquad 2$$

If it is further assumed that the fluid is incompressible then the divergence of the velocity field will be zero, reducing Eq. 2 to the version used in this study:

$$D\vec{\nabla}^2 C - \vec{v} \cdot \vec{\nabla} C = 0 \qquad\qquad 3$$

This equation was solved using a finite difference method on the implicit cubic mesh defined by the 3D tomographic images. Using finite differences, Eq. 3 can be described by the following two terms: The second derivative of concentration (Eq. 4) is defined using a $2^{nd}$ order accurate central difference scheme while the first derivative (Eq. 5) was determined using a $1^{st}$ order-accurate forward or backward difference scheme. Eq. 5 shows a forward difference scheme. In the following equations, $d_l$ is the size of the lattice in real units [m] and $C_{x,y,z}$ is the concentration at the coordinates (x,y,z) in mol·m$^{-3}$.

$$D\vec{\nabla}C = \frac{D}{d_l^2}(C_{x-1,y,z} - 2C_{x,y,z} + C_{x+1,y,z}) + \frac{D}{d_l^2}(C_{x,y-1,z} - 2C_{x,y,z} + C_{x,y+1,z})$$
$$+ \frac{D}{d_l^2}(C_{x,y,z-1} - 2C_{x,y,z} + C_{x,y,z+1}) \qquad\qquad 4$$

$$\vec{v} \cdot \vec{\nabla}C = \frac{v_x}{d_l}(C_{x+1,y,z} - C_{x,y,z}) + \frac{v_y}{d_l}(C_{x,y+1,z} - C_{x,y,z}) + \frac{v_z}{d_l}(C_{x,y,z+1} - C_{x,y,z}) \qquad 5$$

The use of forward or backwards differences is determined according to the principal of upwind advection. Even at the low Reynolds numbers used in this study, the concentration of material in a finite volume will be largely determined by the velocity-driven flux from the finite volume directly upstream from it. This can be implemented by looking at the sign of the velocity component in each direction, if the velocity is negative, forward differentiation is used and vice versa.

A heterogeneous, first-order reaction was implemented at the boundaries where the flow interacts with fiber elements. This boundary condition is applied at every fiber face that touches a fluid element. The boundary condition represents Fickian diffusion from the bulk to the surface of the reacting fiber and can be seen in Eq. 6.

$$D\frac{\partial C}{\partial x} = k_0 C_{surf} = r \qquad\qquad 6$$

where $k_0$ is the reaction coefficient [m·s$^{-1}$], and $C_{Surf}$ is the electrolyte concentration [mol·m$^{-3}$] at the surface of the fiber, which together give the reaction rate, $r$ [mol·m$^{-2}$·s$^{-1}$]. The direction 'x' varies according to which face of the finite volume the fluid element was touching. When discretized Eq. 6 becomes:

$$\frac{D}{2d_l}(C_{x+1,y,z} - C_{x,y,z}) = k_0 C_{x,y,z} \qquad\qquad 7$$

where $C_{x,y,z}$ is the concentration at the fiber surface and $C_{x+1,y,z}$ is a fluid element that exchanges mass with its 'x-face'. This equation is simultaneously solved for each additional face exchanging mass. The mass

transfer coefficient can be computed directly from the reaction rate at these boundaries. The mass transfer coefficient, $k_m$, is defined implicitly from the film theory of mass transfer [11].

$$N_C = k_m A (C_{bulk} - C_{surf}) \qquad\qquad 8$$

Where $N_C$ is the molar flux of electrolyte [mol·s$^{-1}$] being consumed at the surface of the fibers, $A$ is the effective surface area [m$^2$] for mass transfer, and $C_{bulk}$, the bulk concentration is defined as the inlet concentration into the reacting domain. The flux of the reactant has been specified by the RHS of Eq. 7, specifically by multiplying it by the effective mass transfer area, which yields Eq. 9.

$$k_m = \frac{k_0 C_{surf}}{C_{bulk} - C_{surf}} = \frac{r}{C_{bulk} - C_{surf}} \qquad\qquad 9$$

Application of this equation to correctly controlled experimental conditions can yield the mass transfer coefficient, which is the basis of LCDT. For LCDT to be experimentally feasible, there are several assumptions that must be satisfied. The bulk concentration must be known, which in a reactive system is taken to be the concentration far away from the reactive surfaces is. Experimentally, $C_{bulk}$ is taken as the concentration of the inlet fluid and cross-checked by ensuring that the outlet concentration has not changed significantly. This is typically accomplished by applying a high flow rate, which is why most experimentally determined correlations are only applicable for higher Reynolds numbers. $C_{surf}$ is maintained at 0 by applying a high voltage to the electrochemical reaction such that mass transfer limiting conditions are achieved. This tends to result in high reaction rates, which further exacerbates the need for high flows to maintain a constant bulk concentration. The determination of $r$ requires measuring the current produced by the reaction and converting current to molar rate, $n$, using Faraday's Law of Electrolysis:

$$n = \frac{i}{zF} \qquad\qquad 10$$

where $i$ is current [A, or C·s$^{-1}$], $z$ is the number of electrons transferred in the reaction, and $F$ is Faraday's constant [C·mol$^{-1}$]. Thus, the parameters in Eq. 9 are fully measured and/or controlled in a LCDT experiment; however, as pointed out this constrains the conditions to higher Reynolds numbers than those used in practical flow battery operation. Moreover, when small fibers are used to obtain a high surface area per unit volume, the problem of excessive reactant consumption is even more acute.

By using pore-scale modeling the present work can overcome the practical limitations of the experimental approach. Firstly, the reaction was only 'turned on' in small sections of the electrode at once, which prevented excessive consumption of the reactant thereby ensuring 'bulk' concentration was constant.

These reacting sections were non-overlapping, randomly selected cubic areas of the domain, approximately five fiber diameters in edge length (34 voxel edges). Figure 3 shows an example of fluid flowing through a fibrous material, with the red boxes outlining the regions where the reaction was active. The active regions were divided into 'slices' of 16 regions. Each reactive region is randomly oriented near the center of what would be a 4 × 4 grid so they were not always equidistant from one another. This was implemented to prevent only sampling one specific region as more slices were added. Previous work [23] has shown that the these materials can be subject to considerable channeling in the direction of flow. Adding slight randomization in the reactive regions in the simulation prevented over-sampling these features. Each 'slice' of regions was solved independently to minimize the solution domain and reduce computational effort. Secondly, since the concentration in each mesh element was known from the simulation, it was not necessary to ensure $C_{surf} = 0$. This means that a slower reaction rate can be applied that does not necessarily result in mass transfer limited reaction conditions, since the driving force to each surface site can be found from the computed concentration field. A slow reaction rate was accomplished by using a Damköhler number of 0.1 for all simulations. The Damköhler number is a dimensionless number that relates the reaction timescale with the transport timescale. Given that these systems are highly advective, its Damköhler number can be approximated as:

$$Da = \frac{k_0}{U_{AVG}}$$ 11

where $U_{AVG}$ is the average magnitude of the interstitial velocity in the domain [m·s$^{-1}$]. This condition was enforced to prevent overly quick consumption of the reacting species, as the rate of reaction should be 1/10$^{th}$ of that of the material advecting through the domain. Simulations were also performed with Da = 1 and Da = 0.01 and the results suggested the same correlations as with Da = 0.1. The middle value was chosen because at Da = 0.01 the reaction rate was so low at low velocities that an almost imperceptible amount of reactant was consumed. Similarly for Da = 1, at high velocities there was such quick consumption of the reactant that assuming the bulk concentration was the inlet concentration was no longer valid.

One mass transfer coefficient was determined for each reactive zone by solving Eq. 9 for an average surface concentration in that region and using the inlet concentration as the bulk concentration. A further example of the reacting flow can be seen in Figure 4; here, the streamlines have been colored according to the local concentration.

Two parameters were varied to generate a complete data set. The first was the Péclet number, which describes the ratio of advective to diffusive mass transport according to:

$$Pe = \frac{U_{sf} d_f}{D}$$

12

where $d_f$ is the fiber diameter [m] and $U_{sf}$ is the superficial velocity through the material [m·s⁻¹]. For these simulations, specifying the Péclet number determined the reactant diffusivity for that simulation and was varied between 2 and 10 to ensure that at one extreme, the system was far more advective than diffusive (Pe = 10) and at the other the two phenomena were approximately equivalent (Pe = 2) while still maintaining the validity of the upwind advection scheme (Pe ≥ 2). The other macro property that was varied was the instantiating force applied in the Lattice Boltzmann simulations, which is effectively varying the Reynolds number. This force is a dimensionless lattice body force and is analogous to the pressure drop in the real domain and increasing this force leads to higher interstitial velocities through the material. The force was varied from $5\times10^{-9}$ to $5\times10^{-4}$ at logarithmic increments of half an order of magnitude (i.e., $5\times10^{-9}$, $1\times10^{-8}$, $5\times10^{-8}$...).

## 3. Results

### 3.1. Analysis of Tomographic Images

Obtaining an accurate fiber diameter for each material was crucial for the accuracy of the study because the fiber diameter acts as the characteristic length when determining dimensionless quantities such as Reynolds, Schmidt and Péclet numbers. The effective fiber diameter for each material was extracted using a local thickness algorithm on the fiber space as previously reported [23]. The electrospun materials had very similar sized fibers, 1.95 µm and 1.65µm for the unaligned and aligned materials respectively. The carbon felt's diameter was significantly larger at 8.24 µm. As all results are reported as dimensionless quantities, this discrepancy in size increases the robustness of the correlations.

Another key property to consider is the porosity of the material and of the modelling domains. Table 1 lists the maximum, minimum and sample porosity for the modelled materials. The minimum and maximum values refer to the set of all modelled domains, while the sample porosity refers to the porosity of the entire imaged material. There is very little deviation between materials which means that morphological variations between the samples are being defined by the fiber size and anisotropy.

Chords were applied to the pore and fiber space of all three images and the length of each chord was extracted and binned using tools in the PoreSpy toolkit [33]. The resulting distributions can be seen in Figure 5 for the pore-space and Figure 6 for the fiber-space. To prevent skewing of the distributions towards small chords, which appear with high frequency but do not represent the actual size of the pore space, some normalization was applied. The y-axis shows the total length of all chords of a given size, divided by the total length of all chords in that direction in the image. This is plotted versus the logarithm of chord length. For example, if there were 40 chords of length 10 in an image with a total chord length of 200000, that entry would y = 40 × 10 = 400/200000 = 0.002 versus x = log(10) = 1.

The chord length distributions in the pore space provide some useful insights. The peak of every distribution details the expected pore size in that direction. For example, for the aligned electrospun materials the expected pore size would be 10 μm × 16 μm × 11 μm for x,y,z respectively. This suggests the average pore is 50% longer in one direction than the others, which is an expected property of anisotropic media. A quick study of that distribution also shows that there are significantly more pores longer than 30 μm in the y-direction compared to the other directions. The carbon felt shows largely the same distribution in each direction as would be expected of an isotropic material. The unaligned electrospun material does not perform exactly as anticipated, with expected pore sizes of 22 μm, 17 μm and 15 μm for x,y and z respectively. This indicates some minor alignment in the in-plane (x) direction. The permeability results seen in Table 3 support this assertion.

The chord length distributions in the fibers present interesting results. Each material in every direction has a distinct peak in the bin that contains that material's fiber diameter. The only exception to this is the in-plane (y) direction for the aligned material. The peak here is broad and contains chords from length 1.2 – 2.18 μm. This is the only direction that is experiencing two planes of anisotropy, meaning that the fibers are aligned with the y-axis, leading to the drastically different distribution seen here. The rest of this distribution shows significantly longer chords, with a noticeable contribution past 10 μm, whereas the other two directions effectively have no chords longer than 7 μm. These results represent the expected distribution for an aligned electrospun material.

The distributions in the carbon felt fibers also closely match what would be expected from the material's microstructure. As predicted, this woven material is virtually indistinguishable in each direction and apart from the sharp peak at the fiber diameter, there are not any features of interest. The unaligned electrospun material's distribution is more descriptive. All three distributions share the same peak at 1.8 μm but the peak is highest in the z-direction, followed by y then x. This is indicative of a planar material,

as expected, with isotropic fibers in the in-plane directions. The shapes of the in-plane curves also support this, with a flatter peak and a more gradual descent among the in-plane components.

## 3.2. Comparison with other correlations

The data generated in the simulation were compiled and compared to several relevant correlations. A summary of these correlations may be found in Table 2. Figure 7 shows these correlations overlaid on the data from the present simulations, along with a line of best fit through the present data for comparison. For the purposes of these comparisons, the formulation of the Reynolds number used is the same as presented in the original manuscript. For example, You et al. define Reynold's number by the interstitial velocity, so the data presented in Figure 7 reflects this. These studies were performed at high Reynolds numbers so that the systems would have high interstitial velocities and the advective forces would dominate the mass transfer process. All the correlations are in rough agreement with the data, but show increasing disagreement at lower Reynolds numbers, which is to be expected when extrapolating a correlation so far beyond its range of validity. This clearly justifies the present work, since errors as large as an order of magnitude would be incurred by using even the best fitting correlation of Yang and Cussler. In all the presented correlations, the effect of Schmidt number was not actually varied experimentally, but only included as $Sc^{1/3}$, which is the conventional dependence. In the present work, the Schmidt number was varied indirectly by changing the Péclet number, so including this dependence may have also helped improve the line of best fit shown in Figure 7, especially given the importance of diffusive effects in these low Re systems. More detailed analysis of this fitting is given below.

## 3.3. Linearization and Correlation

Literature suggests that the mass transfer properties of a material should be a function of the system's Reynolds and Schmidt numbers. This form is usually referred to as the Generalized Lévêque Equation (GLE) [34]. Definitions of the GLE as well as the Sherwood, Reynolds and Schmidt numbers can be seen below in Equations 13, 14 ,15, and 16 respectively.

$$Sh = A \, Re^{\alpha} \, Sc^{\beta} \qquad \qquad 13$$

$$Sh = \frac{k_m d_f}{D} \qquad \qquad 14$$

$$Re = \frac{U_{sf} d_f}{\nu} \qquad \qquad 15$$

$$Sc = \frac{\nu}{D} \qquad \qquad 16$$

where $U_{sf}$ is the superficial velocity [m·s$^{-1}$] and all $\alpha$ and $\beta$ are the dimensionless fitting parameters used for the Reynolds and Schmidt numbers respectively.

To linearize the data the following grouped parameter was used:

$$\text{Grouped Parameter} = \text{Re}^{\phi} Sc^{\theta} \qquad\qquad 17$$

The coefficients $\phi$ and $\Theta$ were determined via optimizing the linear fit through the data. Using the slope and y-intercept of this line, it can be shown that this can be represented as a GLE of the form:

$$k_M = e^b Re^{\phi m} Sc^{\theta m} \qquad\qquad 18$$

where $m$ and $b$ are the slope and y-intercept respectively.

Figure 8 shows the logarithm of the grouped parameters for each case plotted against the logarithm of the mass transfer coefficient. The results are linear, suggesting the GLE approach is adequate. Table 3 summarizes the grouped parameters plotted in Figure 8 and shows the correlation determined for the mass transfer coefficient. The data was linearized in the same way but using the dimensionless Sherwood number in place of the mass transfer coefficient. In all cases, the final GLE had the form:

$$Sh = \left(\frac{d_f}{\nu}\right) e^b Re^{\phi m} Sc^{\theta m + 1} \qquad\qquad 19$$

The final correlations for the Sherwood number are also listed in Table 3. Analysis of covariance was performed on each regression and the mean standard deviation across all samples of the slope and intercept were $\sigma_{slope}$ = 0.000648 and $\sigma_{intercept}$ = 0.00872 respectively.

## 4. Discussion

Table 3 presents mass transfer correlations presented in terms of both the mass transfer coefficient and the dimensionless Sherwood number. When correlated by the mass transfer coefficient, there is some discrepancy between materials. The exponents on the Reynolds number and the Schmidt number are relatively constant but the pre-factor ('A' from Eq. 13) varies between materials. However, when the correlation is transformed to relate the Sherwood number, these material differences disappear because the effect of the fiber diameter is included in the correlation. The final Sherwood correlations are very similar across all materials, as expected, since dimensionless numbers should be independent of scale. These correlations are also very similar in scale to the correlations discussed earlier [21,22].

To quantify the effects of alignment, the three principal planes of each material were modelled and analyzed. The permeability coefficient for each material in each direction is listed in Table 3. When

analyzed individually, the materials did not all exhibit the expected trends. The hashed data in Figure 9 shows how each directional component of the permeability tensor varies against the average for that material. The behavior of the aligned material is exactly as expected. The through-plane direction has the lowest permeability and is followed by the in-plane (x) direction (representing flow perpendicular to the fibers). The highest permeability is for flow parallel to the fibers, which is the in-plane (y) direction. Theoretically, for perfectly aligned fibers, the in-plane (x) component and the through-plane component would be equal, but for 'moderately aligned' materials a noticeable difference is expected and acceptable. Conversely, the same trend is not seen in the other two materials. The through-plane component of the unaligned material showed the lowest permeability; however, the two in-plane components were also quite different from one another. In the carbon felt material, the in-plane (y) component was much higher than the other directions, despite being theoretically isotropic. It is unclear exactly why these deviations from ideality exist, but a likely cause would be the random sampling and small sample sizes. Because carbon felt is a woven material, it has regions of high anisotropy, but the collective whole should be anisotropic. Unfortunately, this property also makes it susceptible to significant local changes in material properties as previously reported [17].

The solid bars in Figure 9 show the Sherwood number calculated from the correlations shown in Table 3 at a high Reynolds number (Re = 0.9). As with the permeability, the bars represent the deviation from the sample mean, to show how the mass transfer changes in the different planes of the material. Materials with lower permeability should have better mass transfer and vice versa. Low permeability indicates that the material is more constricted, which hinders flow but enhances mixing. The permeability is low because the electrolyte encounters many solids, which obstruct the flow. Conversely, these same obstructions facilitate mass transfer, giving the electrolyte surfaces to diffuse to. Having more of them in a smaller area increases mixing, resulting in a thinner mass transfer boundary layer, and enhancing mass transfer rates. Figure 9 shows exactly this trend. In all cases, the positive deviation of permeability is proportional to the negative deviation in the predicted Sherwood number.

Figure 9 presents the deviations on a sample basis, with each direction analyzed as a function of the other two directions. Figure 10 (left) presents the permeability and Sherwood number by plotting the Sherwood number according to the correlations in Table 3 versus the Reynolds number for $10^{-6} \leq$ Re < 1.0. The lines are colored according to their permeability (on a log scale), as indicated by the color bar at the right of the figure. The trend is very clear and matches what was shown in Figure 9: as the permeability decreases the Sherwood number increases. The grouping of the data presented in Figure 10 (left) also suggests that

general Sherwood correlations can be defined depending on the structure of the material and relative direction of flow. Flow in isotropic materials encompasses all planes for the carbon felt material as well as the in-plane components of the unaligned electrospun material. Grouping the data together and optimizing the fit as before suggests the following correlation.

$$Sh_{isotropic} = 0.879Re^{0.402}Sc^{0.390}$$ 20

Further grouping of the through-plane components for the electrospun materials suggests:

$$Sh_{through-plane} = 0.906Re^{0.432}Sc^{0.432}$$ 21

Taking into account the standard deviations of the regressions, the pre-factor constant for the isotropic correlation is 0.879 ± 0.0100 and the pre-factor for the through plane correlation is 0.906 ± 0.00751. The uncertainty contributing to the exponents for the Reynolds and Schmidt numbers for both correlations are not significant, being below $10^{-3}$.

To further illustrate the effect of permeability on the mass transfer coefficient the right side of Figure 10 shows the predicted Sherwood number versus the dimensionless permeability of the materials. The dimensionless permeability of a material is defined as:

$$k_{DIM} = \frac{k}{d_f^2}$$ 22

The dimensionless permeability is useful for comparing materials of different sizes and in this case allows for much simpler comparison between the electrospun materials and the much larger felts. The trend very clearly agrees with what was already stated, but also suggests the effect of permeability on the mass transfer in a material decreases with the Reynolds number. This is significant as the permeability of a material determines the efficacy of moving the bulk electrolyte through the fibrous electrode, whereas the mass transfer coefficient determines how effectively that material can diffuse to the surface of the material to react. A low porosity electrode that utilized aligned fibers perpendicular to the flow of the electrolyte would have superior mass transfer properties, however these would come at the expense of the permeability, which would increase the parasitic pumping load on the cell. The negative relationship between the two suggests the need for optimization to fully exploit the capabilities of the electrode.

## 5. Conclusions

A method was presented for determining the mass transfer coefficient in porous media using direct numerical simulations on 3D tomograms. The velocity field for pressure driven viscous flow was first

determined using the Lattice Boltzmann Method on X-ray computed tomograms of the materials. Subsequently, the advection-diffusion equation was solved on the velocity field, with a heterogeneous reaction consuming electrolyte at the surface of the fibers. The resulting 3D concentration profile through the material was analyzed to determine the local mass transfer coefficient according to the film theory of mass transfer. These simulations were performed at a variety of different pressure driving forces, increasing the flow rate through the material as well as with a variety of different diffusion coefficients to make the results as general as possible.

Three materials relevant to flow battery electrodes were imaged and analyzed. Commercially produced carbon felts represented isotropic materials, one plane of alignment was introduced using electrospun carbon fibers, which are planar and possess two isotropic planes (in-plane) and one anisotropic plane (through-plane). Electrospun carbon fibers with an additional degree of anisotropy (alignment in one in-plane direction) were also used. Each material was analyzed in each of the three principal directions; the through-plane and both in-plane directions. The mass transfer coefficients obtained through these simulations were compared to literature correlations. The data was found to agree very well with literature, especially at high Reynolds numbers, but some literature correlations were erroneous at low Reynolds number.

Mass transfer correlations in the form of the Generalized Lévêque Equation were presented for each material. The correlations related the mass transfer coefficient as well as the Sherwood number to the system's Reynolds and Schmidt numbers. When correlating the mass transfer coefficient directly it was found that the equations were highly dependent on the scale of the system, whereas correlating in terms of the Sherwood number removed this dependence, making the system dimensionless.

A mass transfer correlation in terms of the Sherwood number was proposed for flow in isotropic fibrous media, specifically $Sh = 0.879 \, Re^{0.402} \, Sc^{0.390}$. This correlation is dimensionless and should be valid for flow through fibrous media that exhibits no anisotropy in the direction of flow. A second correlation was proposed for through-plane flow in planar media, or any flow against (perpendicular to) anisotropic media; $Sh = 0.906 \, Re^{0.432} \, Sc^{0.432}$.

The permeability coefficient for each material and each direction was analyzed. The expected characteristics of planar and isotropic materials were not observed in all cases; however, the data convincingly showed that materials with higher permeability possessed a lower Sherwood number and mass transfer coefficient. It was proposed that the same characteristics that determine low permeability,

such as low mean free path in the material and small constricted flow, also promotes mass transfer, increasing the mass transfer coefficient, and vice-versa. The results suggest that further analysis and microstructure optimization are necessary to design an ideal flow battery electrode as the permeability of the material and its mass transfer coefficient are so closely and negatively related.

Pore-scale modeling in voxel-based images can be a useful tool for obtaining experimentally inaccessible transport parameters, even engineering correlations for mass transfer coefficients as shown here. Future efforts in this area should consider extending this approach even further to model cell performance by incorporating all the relevant and coupled physics [35].

## 6. Acknowledgements

## 7. References

[1] K.M. Lisboa, J. Marschewski, N. Ebejer, P. Ruch, R.M. Cotta, B. Michel, D. Poulikakos, Mass transport enhancement in redox flow batteries with corrugated fluidic networks, J. Power Sources. 359 (2017) 322–331. doi:10.1016/j.jpowsour.2017.05.038.

[2] J. Houser, A. Pezeshki, J.T. Clement, D. Aaron, M.M. Mench, Architecture for improved mass transport and system performance in redox flow batteries, J. Power Sources. 351 (2017) 96–105. doi:10.1016/j.jpowsour.2017.03.083.

[3] L.F. Arenas, C.P. de León, F.C. Walsh, Mass transport and active area of porous Pt/Ti electrodes for the Zn-Ce redox flow battery determined from limiting current measurements, Electrochimica Acta. 221 (2016) 154–166. doi:10.1016/j.electacta.2016.10.097.

[4] V.B. Oliveira, D.S. Falcão, C.M. Rangel, A.M.F.R. Pinto, Heat and mass transfer effects in a direct methanol fuel cell: A 1D model, Int. J. Hydrog. Energy. 33 (2008) 3818–3828. doi:10.1016/j.ijhydene.2008.04.032.

[5] H. Ohmori, H. Iwai, Simulation of solid oxide iron-air battery: Effects of heat and mass transfer on charge/discharge characteristics, J. Power Sources. 286 (2015) 264–275. doi:10.1016/j.jpowsour.2015.03.149.

[6] K. Kinoshita, S.C. Leach, Mass-Transfer Study of Carbon Felt, Flow-Through Electrode, J. Electrochem. Soc. 129 (1982) 1993–1997. doi:10.1149/1.2124338.

[7] X. You, Q. Ye, P. Cheng, The dependence of mass transfer coefficient on the electrolyte velocity in carbon felt electrodes: Determination and validation, J. Electrochem. Soc. 164 (2017) E3386–E3394. doi:10.1149/2.0401711jes.

[8] Q. Xu, T.S. Zhao, Determination of the mass-transport properties of vanadium ions through the porous electrodes of vanadium redox flow batteries, Phys. Chem. Chem. Phys. 15 (2013) 10841–10848. doi:10.1039/C3CP51944A.

[9] A. Xu, T.S. Zhao, L. Shi, J.B. Xu, Lattice Boltzmann Simulation of Mass Transfer Coefficients for Chemically Reactive Flows in Porous Media, J. Heat Transf. 140 (2018) 052601. doi:10.1115/1.4038555.

[10] J.D. Milshtein, K.M. Tenny, J.L. Barton, J. Drake, R.M. Darling, F.R. Brushett, Quantifying Mass Transfer Rates in Redox Flow Batteries, J. Electrochem. Soc. 164 (2017) E3265–E3275. doi:10.1149/2.0201711jes.

[11] W.K. Lewis, W.G. Whitman, Principles of Gas Absorption., Ind. Eng. Chem. 16 (1924) 1215–1220. doi:10.1021/ie50180a002.

[12] S. Liu, M. Kok, Y. Kim, J.L. Barton, F.R. Brushett, J. Gostick, Evaluation of Electrospun Fibrous Mats Targeted for Use as Flow Battery Electrodes, J. Electrochem. Soc. 164 (2017) A2038–A2048. doi:10.1149/2.1301709jes.

[13] P. Trogadas, O.O. Taiwo, B. Tjaden, T.P. Neville, S. Yun, J. Parrondo, V. Ramani, M.-O. Coppens, D.J.L. Brett, P.R. Shearing, X-ray micro-tomography as a diagnostic tool for the electrode degradation in vanadium redox flow batteries, Electrochem. Commun. 48 (2014) 155–159. doi:10.1016/j.elecom.2014.09.010.

[14] G. Qiu, C.R. Dennison, K.W. Knehr, E.C. Kumbur, Y. Sun, Pore-scale analysis of effects of electrode morphology and electrolyte flow conditions on performance of vanadium redox flow batteries, J. Power Sources. 219 (2012) 223–234. doi:10.1016/j.jpowsour.2012.07.042.

[15] L.D. Brown, T.P. Neville, R. Jervis, T.J. Mason, P.R. Shearing, D.J.L. Brett, The effect of felt compression on the performance and pressure drop of all-vanadium redox flow batteries, J. Energy Storage. 8 (2016) 91–98. doi:10.1016/j.est.2016.10.003.

[16] R. Jervis, L.D. Brown, T.P. Neville, J. Millichamp, D.P. Finegan, T.M.M. Heenan, D.J.L. Brett, P.R. Shearing, Design of a miniature flow cell for in situ x-ray imaging of redox flow batteries, J. Phys. Appl. Phys. 49 (2016) 434002. doi:10.1088/0022-3727/49/43/434002.

[17] R. Jervis, M.D.R. Kok, T.P. Neville, Q. Meyer, L.D. Brown, F. Iacoviello, J.T. Gostick, D.J.L. Brett, P.R. Shearing, In situ Compression and X-ray Computed Tomography of Flow Battery Electrodes, J. Energy Chem. (n.d.). doi:10.1016/j.jechem.2018.03.022.

[18] Kok Matt D. R., Jervis Rhodri, Brett Dan, Shearing Paul R., Gostick Jeff T., Insights into the Effect of Structural Heterogeneity in Carbonized Electrospun Fibrous Mats for Flow Battery Electrodes by X-Ray Tomography, Small. 14 (2018) 1703616. doi:10.1002/smll.201703616.

[19] T. Li, N.G. Deen, J.A.M. Kuipers, Numerical investigation of hydrodynamics and mass transfer for in-line fiber arrays in laminar cross-flow at low Reynolds numbers, Chem. Eng. Sci. 60 (2005) 1837–1847. doi:10.1016/j.ces.2004.10.032.

[20] L. Bao, G.G. Lipscomb, Well-developed mass transfer in axial flows through randomly packed fiber bundles with constant wall flux, Chem. Eng. Sci. 57 (2002) 125–132. doi:10.1016/S0009-2509(01)00368-2.

[21] E.L. Cussler, Diffusion: Mass Transfer in Fluid Systems, Cambridge University Press, 2009.

[22] M.-C. Yang, E.L. Cussler, Designing hollow-fiber contactors, AIChE J. 32 (1986) 1910–1916. doi:10.1002/aic.690321117.

[23] Kok Matt D. R., Jervis Rhodri, Brett Dan, Shearing Paul R., Gostick Jeff T., Flow Batteries: Insights into the Effect of Structural Heterogeneity in Carbonized Electrospun Fibrous Mats for Flow Battery

Electrodes by X-Ray Tomography (Small 9/2018), Small. 14 (2018) 1870040. doi:10.1002/smll.201870040.

[24] M.D.R. Kok, J.T. Gostick, Transport properties of electrospun fibrous membranes with controlled anisotropy, J. Membr. Sci. 473 (2015) 237–244. doi:10.1016/j.memsci.2014.09.017.

[25] D.S. Eastwood, R.S. Bradley, F. Tariq, S.J. Cooper, O.O. Taiwo, J. Gelb, A. Merkle, D.J.L. Brett, N.P. Brandon, P.J. Withers, P.D. Lee, P.R. Shearing, The application of phase contrast X-ray techniques for imaging Li-ion battery electrodes, Nucl. Instrum. Methods Phys. Res. Sect. B Beam Interact. Mater. At. 324 (2014) 118–123. doi:10.1016/j.nimb.2013.08.066.

[26] S. Torquato, Random Heterogeneous Materials: Microstructure and Macroscopic Properties, Springer Science & Business Media, 2013.

[27] M.D.R. Kok, A. Khalifa, J.T. Gostick, Multiphysics Simulation of the Flow Battery Cathode: Cell Architecture and Electrode Optimization, J. Electrochem. Soc. 163 (2016) A1408–A1419. doi:10.1149/2.1281607jes.

[28] M.M. Tomadakis, T.J. Robertson, Viscous Permeability of Random Fiber Structures: Comparison of Electrical and Diffusional Estimates with Experimental and Analytical Results, J. Compos. Mater. 39 (2005) 163–188. doi:10.1177/0021998305046438.

[29] N. Satofuka, T. Nishioka, Parallelization of lattice Boltzmann method for incompressible flow computations, Comput. Mech. 23 (1999) 164–171. doi:10.1007/s004660050397.

[30] Palabos, FlowKit Ltd, n.d. http://www.palabos.org/.

[31] M. Januszewski, M. Kostur, Sailfish: A flexible multi-GPU implementation of the lattice Boltzmann method, Comput. Phys. Commun. 185 (2014) 2350–2368. doi:10.1016/j.cpc.2014.04.018.

[32] W. Degruyter, A. Burgisser, O. Bachmann, O. Malaspinas, Synchrotron X-ray microtomography and lattice Boltzmann simulations of gas flow through volcanic pumices, Geosphere. 6 (2010) 470–481. doi:10.1130/GES00555.1.

[33] PoreSpy, PMEAL, Unversity of Waterloo, n.d.

[34] H. Martin, The generalized Lévêque equation and its practical use for the prediction of heat and mass transfer rates from pressure drop, Chem. Eng. Sci. 57 (2002) 3217–3223. doi:10.1016/S0009-2509(02)00194-X.

[35] A. Xu, W. Shyy, T. Zhao, Lattice Boltzmann modeling of transport phenomena in fuel cells and flow batteries, Acta Mech. Sin. 33 (2017) 555–574. doi:10.1007/s10409-017-0667-6.
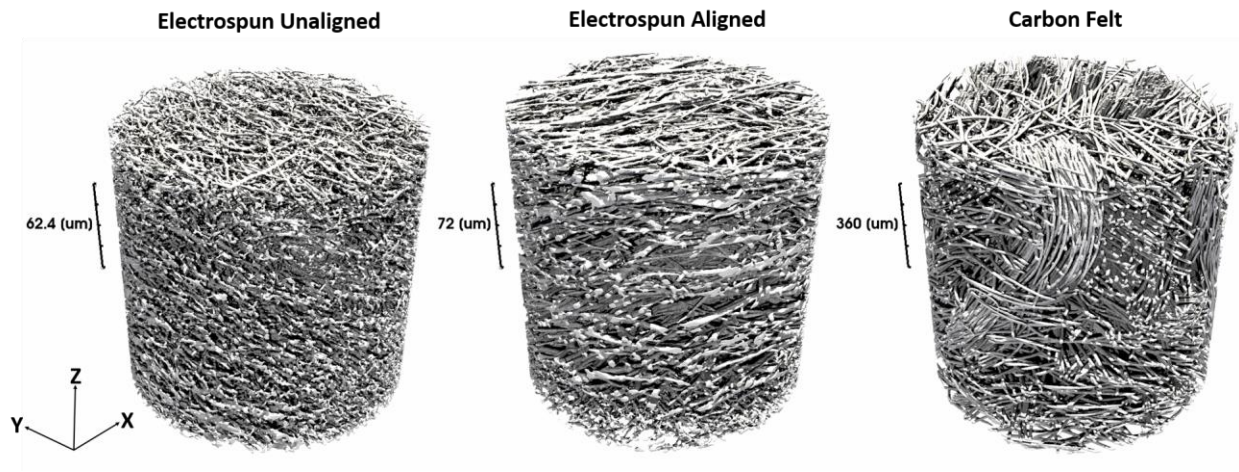
# 8. Figures and Tables



Figure 1: Reconstructed 3D image from X-ray computed tomography. The left image shows the electrospun unaligned material, the middle image shows the electrospun material with anisotropic fibers, the commercially available carbon felt is shown on the right. Note the substantially larger scale bar of the carbon felt image compared to the electrospun materials.
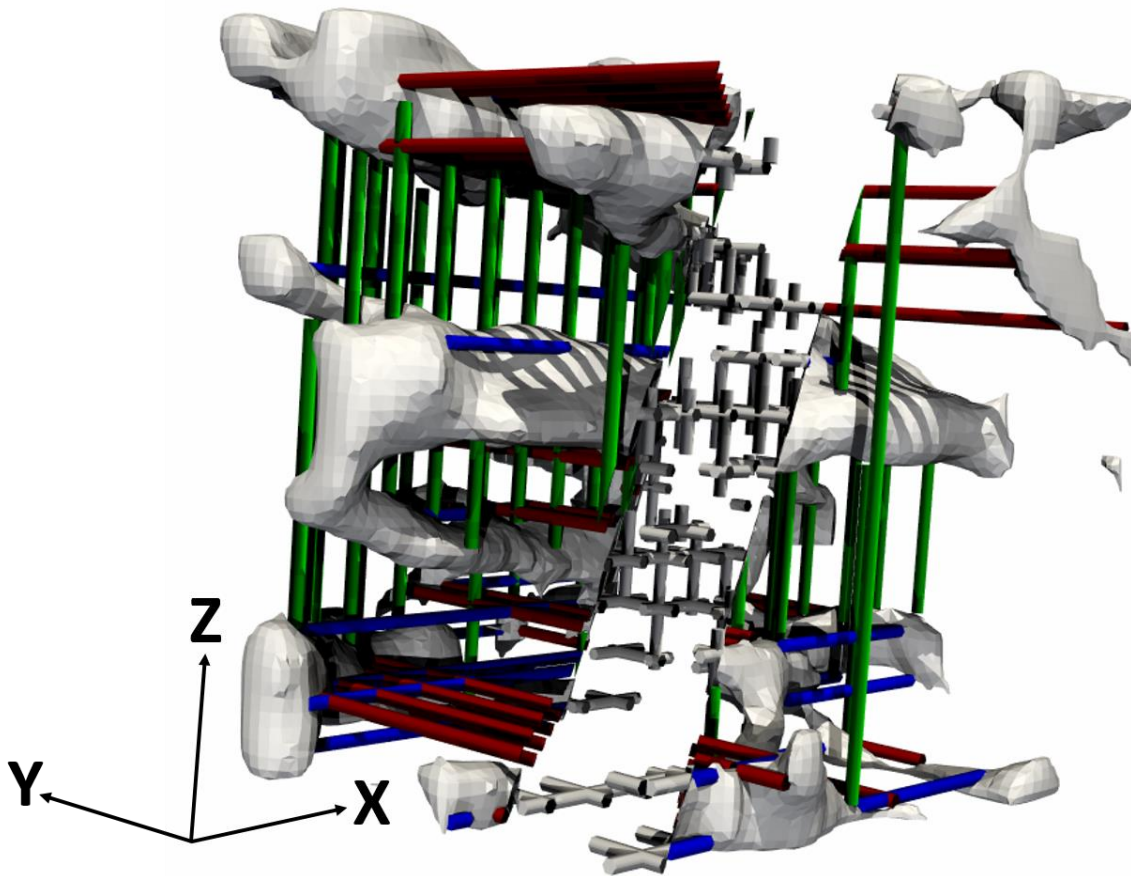
Figure 2: Example of chords applied to pore space and fiber space in the electrospun material. The blue, red, and green chords represent the x,y and z chords in the pore space respectively. The cutout in the middle of the image shows the chords applied to the fiber phase (all grey)
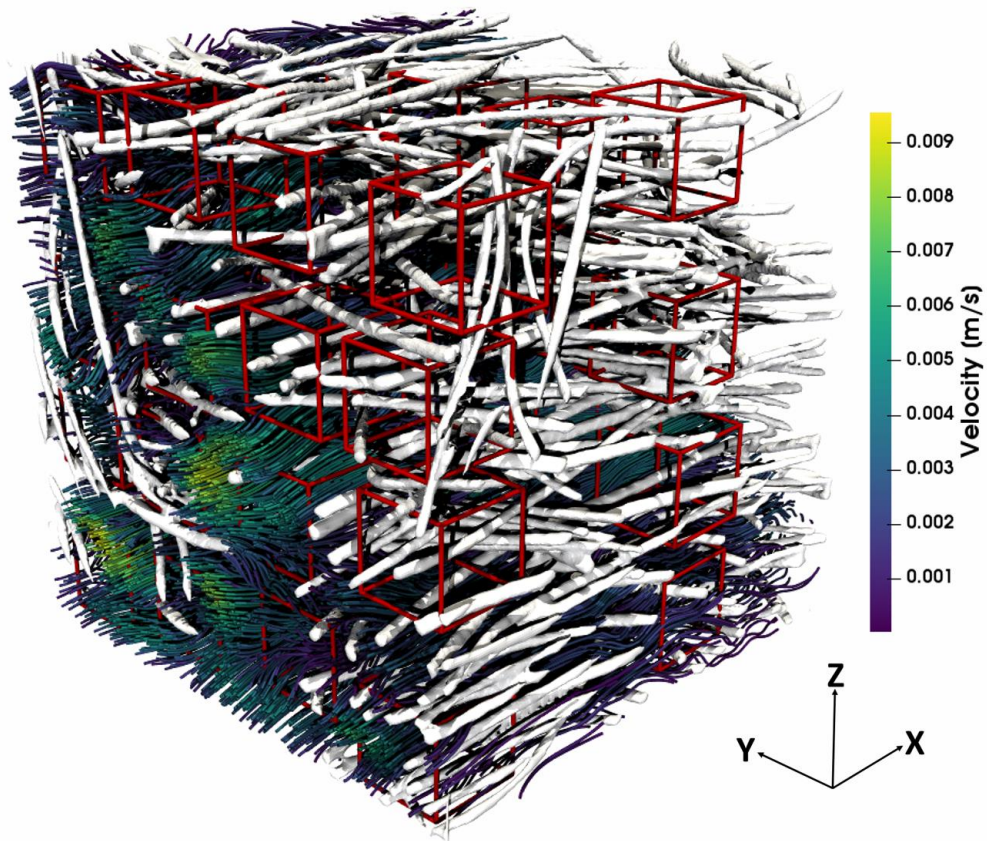
Figure 3: Representative flow domain with the streamlines being colored according to velocity. The streamlines have been cut out to better show the fibers and the reacting domains which are shown as red boxes. This is a sample data set, showing where the mass transfer coefficient was determined. All simulations were performed on a single 'slice' of reactive regions, but multiple simulations were performed per sample
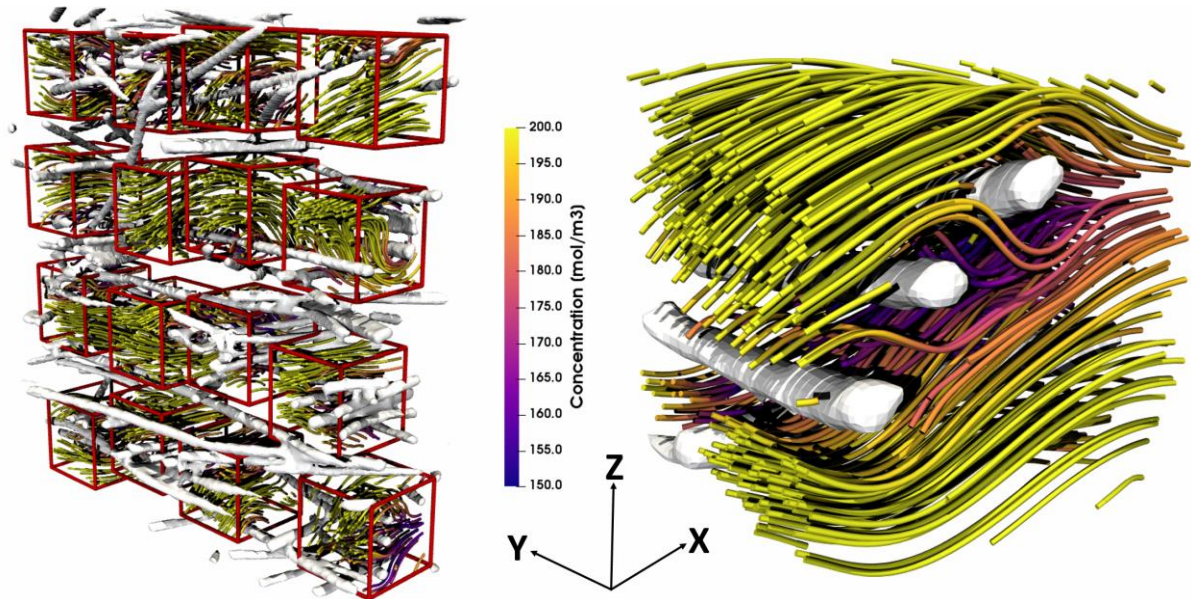
Figure 4: Example of the reacting regions solved for in the simulations. The left side shows one slice of regions, equivalent to one solution domain and the right side shows a more detailed simulation on one region. In this case the streamlines are colored according to the solution concentration [mol·m$^{-3}$] at the point in the flow.

Table 1: Minimum, maximum and sample porosities for the materials modelled. The minimum and maximum values were determined on an individual modelling domain basis while the sample porosity refers to the porosity of the sample as a whole.

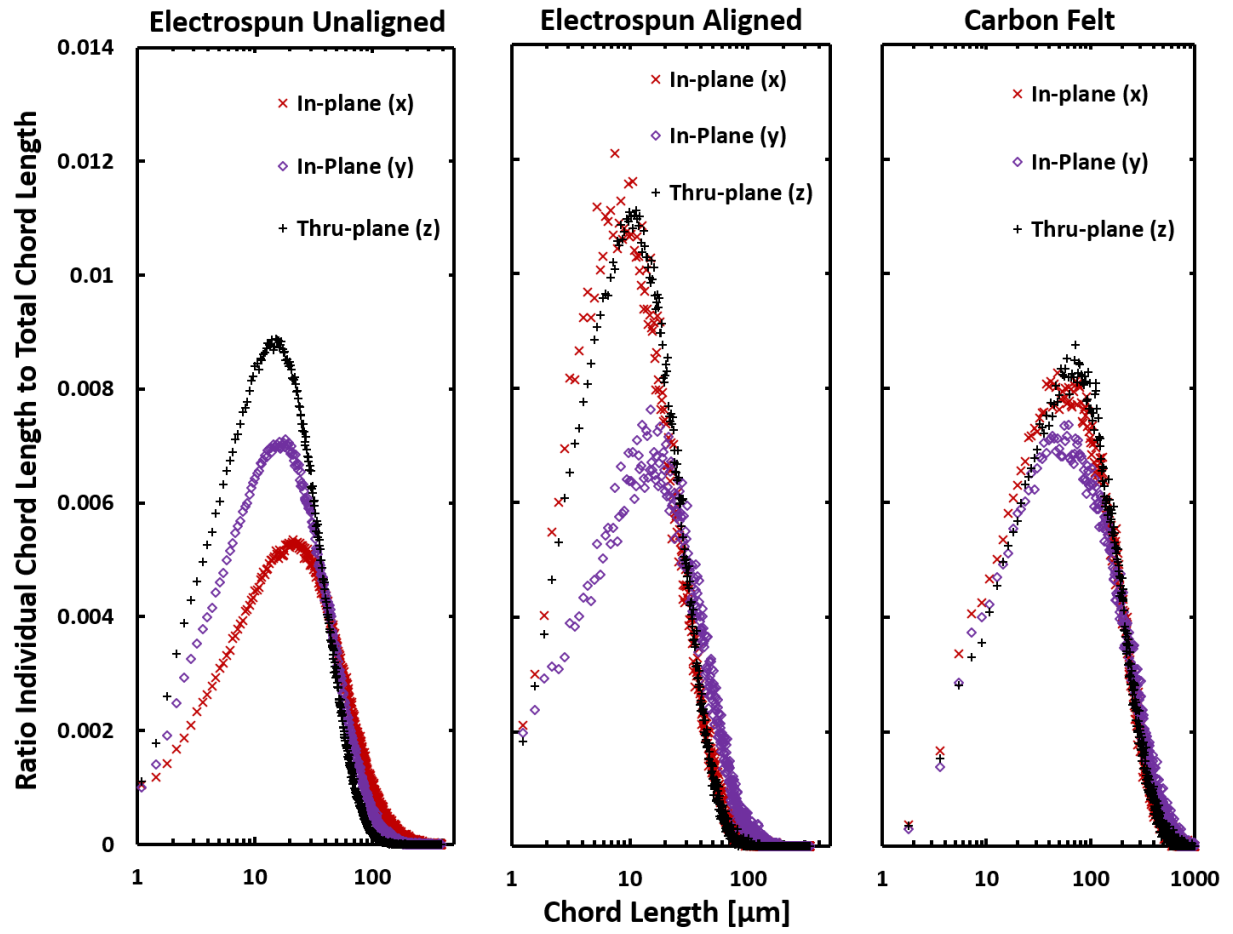| MATERIAL | POROSITY | | |
|---|---|---|---|
| | Minimum | Maximum | Sample |
| Electrospun Unaligned | 0.8825 | 0.9186 | 0.9010 |
| Electrospun Aligned | 0.8786 | 0.9165 | 0.9006 |
| Carbon Felt | 0.8710 | 0.9257 | 0.9005 |

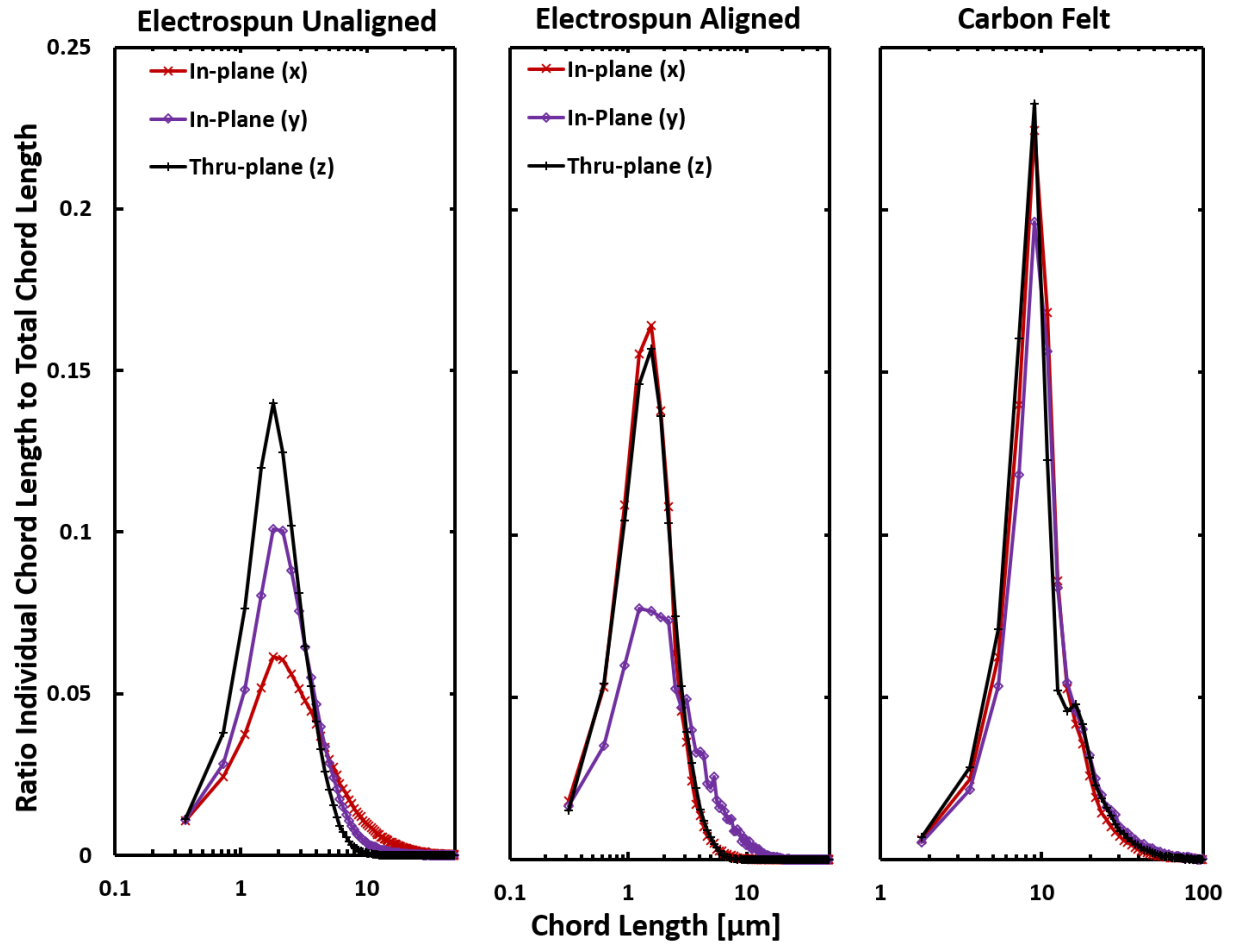Figure 5: Chord-length distribution in the pore-space for the three materials.

Figure 6: Chord-length distributions in the fiber-space for the three materials.

Table 2: Summary of selected correlations for mass transfer coefficients through fibrous materials

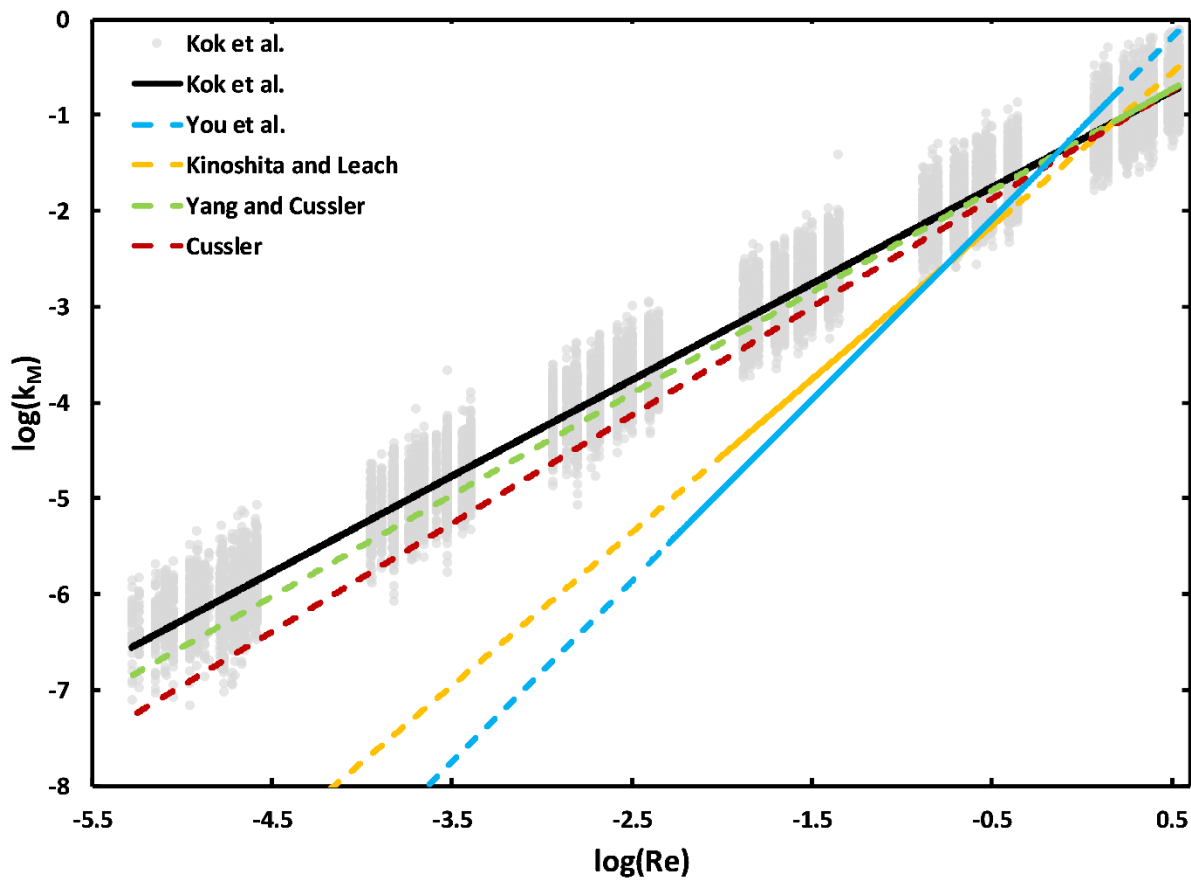| Author | Correlation | Reference |
|---|---|---|
| You et al. | $Sh = 1.68Re^{0.9}$ | [7] |
| Kinoshita and Leach | $Sh = 1.101Re^{0.61}$ | [6] |
| Yang and Cussler | $Sh = 0.9Re^{0.40}Sc^{0.33}$ | [22] |
| Cussler | $Sh = 0.8Re^{0.47}Sc^{0.33}$ | [21] |

Figure 7: Comparison of mass transfer coefficient from selected correlations to mass transfer coefficient determined by the direct numerical simulation. All data presented was gathered from carbon felts excluding the Cussler correlation which was intended for "capillary beds" The grey background data shows the results from this study and the other data is presented as lines of best fit from other correlations. The dotted lines represent regions where the correlation has been extrapolated.
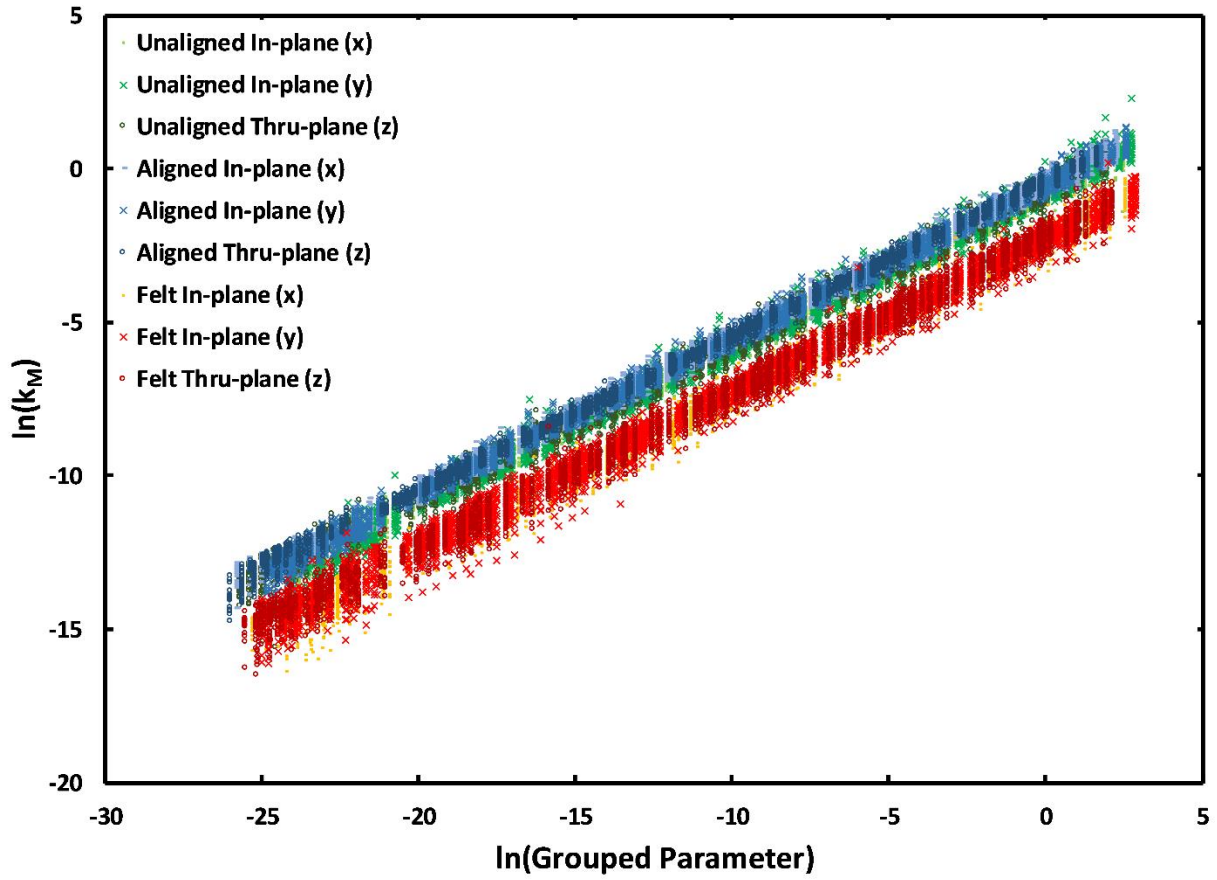
Figure 8: Natural logarithm of the mass transfer coefficient versus natural logarithm of the grouped parameter for all materials in all directions.

Table 3: Summary of grouped parameters and individual correlations for each material and each direction.

| Material and Direction | Grouped Parameter | Correlation for $k_M$ | Correlation for Sh | Permeability [m²] |
|---|---|---|---|---|
| Unaligned IP (x) | $Re^{0.787}Sc^{-1.21}$ | $0.467Re^{0.398}Sc^{-0.612}$ | $0.904Re^{0.398}Sc^{0.388}$ | $3.61\times10^{-12}$ |
| Unaligned IP (y) | $Re^{0.784}Sc^{-1.21}$ | $0.489Re^{0.400}Sc^{-0.615}$ | $0.948Re^{0.400}Sc^{0.385}$ | $2.81\times10^{-12}$ |
| Unaligned TP (z) | $Re^{0.840}Sc^{-1.16}$ | $0.464Re^{0.420}Sc^{-0.579}$ | $0.899Re^{0.420}Sc^{0.421}$ | $1.79\times10^{-12}$ |
| Aligned IP (x) | $Re^{0.853}Sc^{-1.15}$ | $0.650Re^{0.430}Sc^{-0.578}$ | $0.926Re^{0.430}Sc^{0.422}$ | $1.48\times10^{-12}$ |
| Aligned IP (y) | $Re^{0.846}Sc^{-1.16}$ | $0.587Re^{0.426}Sc^{-0.583}$ | $0.836Re^{0.426}Sc^{0.417}$ | $1.75\times10^{-12}$ |
| Aligned TP (z) | $Re^{0.882}Sc^{-1.11}$ | $0.640Re^{0.443}Sc^{-0.558}$ | $0.912Re^{0.443}Sc^{0.442}$ | $1.04\times10^{-12}$ |
| Felt IP (x) | $Re^{0.782}Sc^{-1.17}$ | $0.104Re^{0.403}Sc^{-0.604}$ | $0.855Re^{0.403}Sc^{0.396}$ | $4.90\times10^{-11}$ |
| Felt IP (y) | $Re^{0.812}Sc^{-1.22}$ | $0.103Re^{0.409}Sc^{-0.615}$ | $0.841Re^{0.409}Sc^{0.385}$ | $8.59\times10^{-11}$ |
| Felt TP (z) | $Re^{0.794}Sc^{-1.20}$ | $0.104Re^{0.400}Sc^{-0.603}$ | $0.849Re^{0.400}Sc^{0.397}$ | $5.50\times10^{-11}$ |
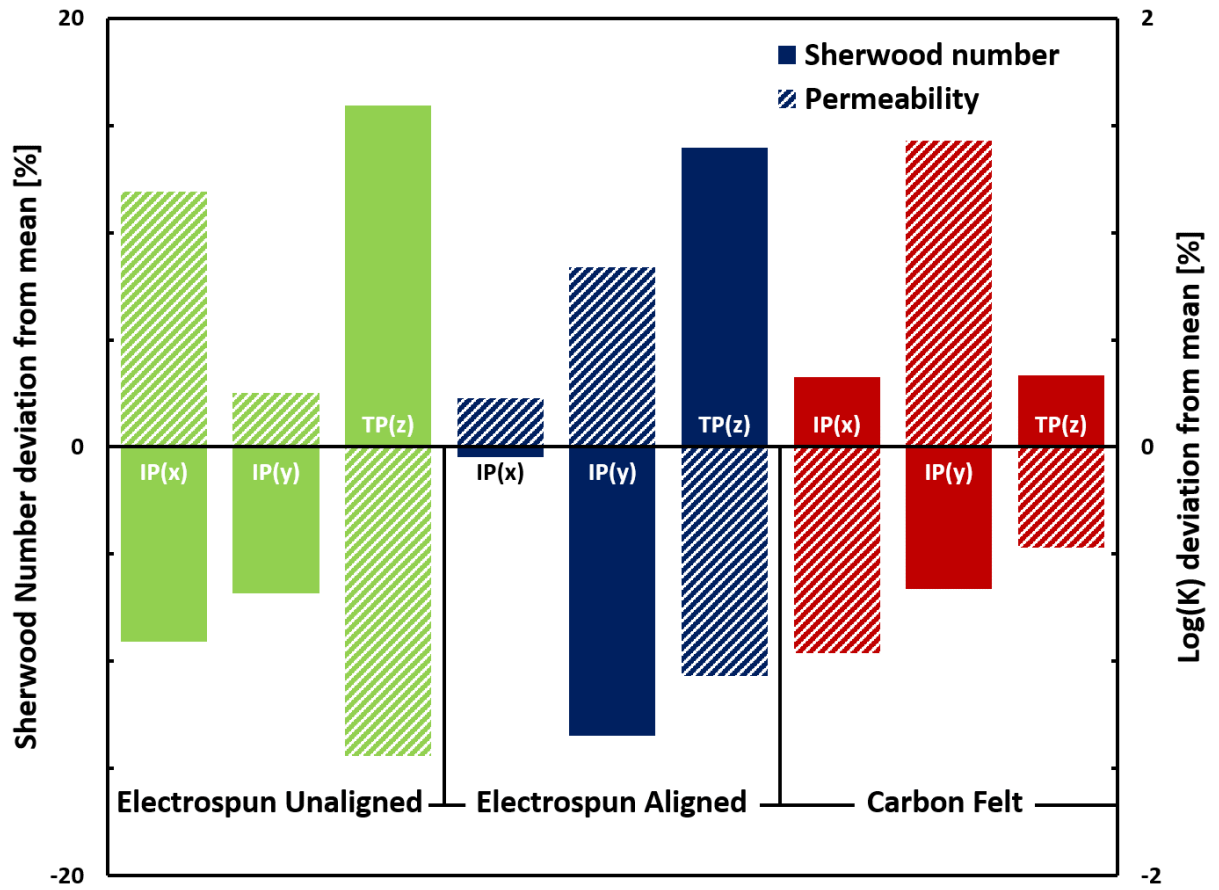
Figure 9: Deviation from the mean as a percentage. Each of the three samples has its own mean. The solid bars represent the Sherwood number (by correlation) for high Reynolds number (Re = 0.9). The hashed bars the logarithm of the permeability coefficient for the material.
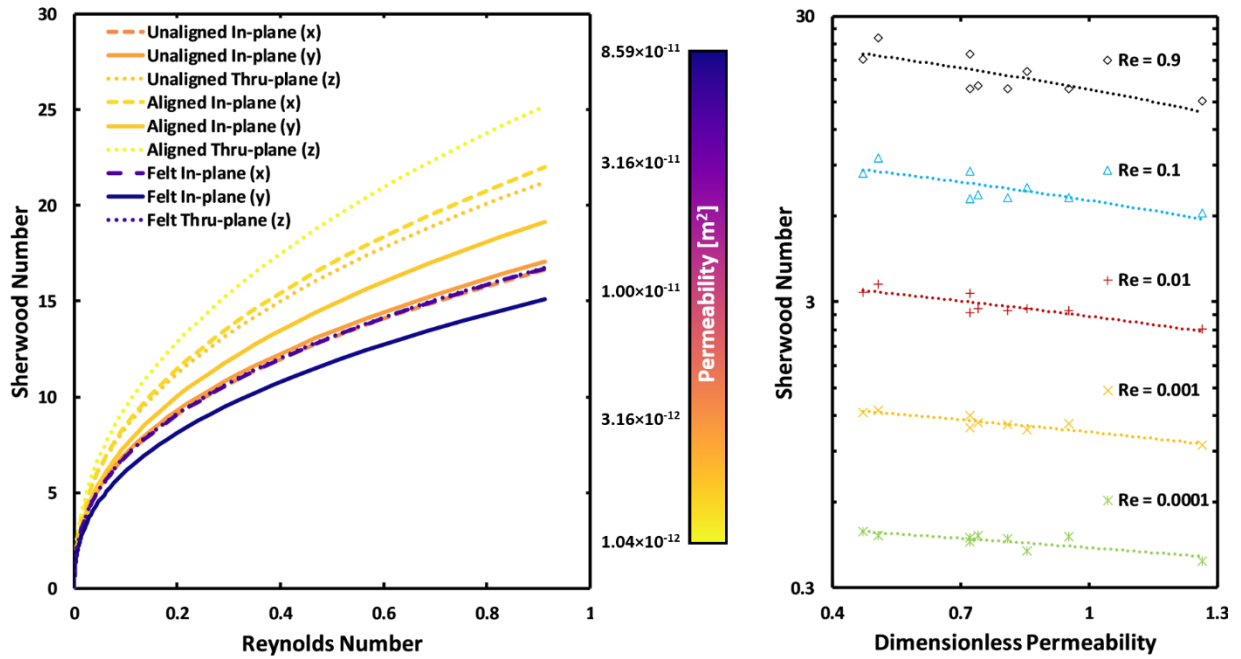
Figure 10: (Left) Sherwood number versus Reynolds number for each material. The colors mapped to the material permeability on a log scale. The solid lines are the in-plane (y) components, the dashed lines are the in-plane (x) component and the dotted lines are the in through-plane (z) components. (Right) The predicted Sherwood number versus dimensionless permeability. The lines show the line of best fit through the data set.